Electro-chemo-mechanical effect in Gd-doped ceria thin films with controlled orientation

Santucci, Simone; Zhang, Haiwu; Sanna, Simone; Pryds, Nini; Esposito, Vincenzo

Published in:
Journal of Materials Chemistry A

Link to article, DOI:
10.1039/D0TA05500J

Publication date:
2020

Document Version
Peer reviewed version

Journal of
Materials Chemistry A

Materials for energy and sustainability

Accepted Manuscript

This article can be cited before page numbers have been issued, to do this please use: S. Santucci, H. Zhang, S. Sanna, N. Pryds and V. Esposito, *J. Mater. Chem. A*, 2020, DOI: 10.1039/D0TA05500J.

ROYAL SOCIETY OF CHEMISTRY

rsc.li/materials-a

View Article Online
DOI: 10.1039/D0TA05500J

ARTICLE

Electro-chemo-mechanical effect in Gd-doped Ceria thin films with a controlled orientation

Simone Santucci[a], Haiwu Zhang [a], Simone Sanna [b], Nini Pryds [a], Vincenzo Esposito* [a]*

Gd-doped ceria fluorites (CGO) exhibits prominent electro-chemo-mechanical properties and giant-electrostriction at room temperature has been recently disclosed in both CGO polycrystalline films and bulk. The electromechanical properties in CGO depend on oxygen vacancy defects of the fluorite lattice. Early experiments suggest that defects along the [111] crystallographic direction promote high atomic distortion. These factors result in the largest electrostriction response ever measured. However, only out-of-plane electrostriction (i.e. M_{13}) in (111) CGO oriented thin films has been reported so far, and several questions remain open about electrostriction mechanism in the oxygen-defective fluorite. Here, we present electromechanical performances along with different crystallographic directions. We grow thin films by pulsed laser deposition on single crystals substrates to obtain longitudinal, and shear deformations (*i.e.* M_{11} and M_{12}) of highly coherent (100), (110) and (111) oriented CGO thin films. As a result, we find an order of magnitude higher electrostrictive coefficient along [100]. Such an analysis gives a new insight into the mechanism of CGO electrostriction.

Introduction

Ceria-based materials apply in a wide range of applications such as solid oxide fuel cells (SOFCs) [1–3], oxygen sensors [3,4] and storage[5], catalysts [5–7] and memristors [8–10]. Ceria oxide, i.e. $CeO_{2-\delta}$, is capable of accommodating a high amount of oxygen vacancies ($\mathbf{V_O^{\bullet\bullet}}$) into the lattice, which results in a remarkable versatility as ionic conductor and catalyst [11–13]. At temperatures superior to 1200 °C [14] and low oxygen partial pressure ($p_{O2} \approx 2.5 \times 10^{-3}$ atm) [15], ceria undergoes a chemical reduction of Ce^{4+} to Ce^{3+}releasing oxygen gas and consequently increasing the defects concentration, $\delta = [\mathbf{V_O^{\bullet\bullet}}]$ [5,16]. Acceptor doping, *e.g*. by substitutional rare-earth cations with a 3+ valence state (*i.e.* Gd, Nd, Sm, La), stabilizes the structure and leads to high ionic mobility [2,7,17–21]. At room temperature, doped ceria showed outstanding electromechanical properties due to local distortion in the vicinity of oxygen vacancies [22]. Studies carried out on Gd-doped ceria (CGO) thin films [22–26], bulk [27,28] and membranes [29–31], show an average electrostriction coefficient of $M_e \approx 6 \cdot 10^{-18}$ ($m^2 V^{-2}$) [22], which is comparable to the *state-of-the-art* materials such as $Pb(Mn_{1/3}Nb_{2/3})O_3$ ($M_e = 2 \cdot 10^{-18}$ m^2V^{-2}) [32]. For classical electrostrictors, Newnham *et al*. provided a relationship in which the logarithm of performances depends on *(S/ε)*, with *S* elastic compliance and *ε* dielectric constant [33]. However, Yavo *et al.* [34] showed that CGO electromechanical properties are conflicting with Newnham law. The electrostriction coefficient is two-three orders of magnitude higher than similar materials [35], meaning that a different mechanism is in play. In the same study, they also showed high electrostriction in (Y, Nb)-stabilized Bi_2O_3 bulk. These findings suggest that such features are common to some defective fluorite structures, representing a new family of electromechanical functional materials.

X-ray absorption spectroscopy (XAS) measurements on CGO attribute the electromechanical activity to the lattice distortion in the presence of oxygen vacancies [22,36,37]. Although the dopant has not an active role in the single lattice model [22,36], doping and vacancies association are able to influence the electrostriction in cerium oxide. In polycrystalline CGO, vacancies are mainly controlled by associations at the grain boundaries [38–40], which also act as ionic blocking barriers controlled by the dopant [17,38,41,42]. Under an electric field, if the grain boundaries of the material have high resistivity, the voltage drops correspondingly. As a consequence, the overall electromechanical response drops [30]. However, grain size is not directly related to electrostriction performances as reported in our recent work [27]. We show that the electrostrictive behavior of polycrystalline CGO ceramics depends on the vacancy configurations within the grain boundaries. For these reasons, a grain boundaries-free material is needed to have a clear insight into the sole lattice distortion effect.

To date, only the out-of-plane component of electrostriction i.e. M_{13} has been measured in thin films [23,43]. Here, we apply a top planar electrodes configuration which allows investigating the other electrostriction directions of the matrix i.e. M_{11}, M_{12}. By varying the crystal orientation of the film, we are able to study the crystal distortion at different crystallographic directions.

View Article Online
DOI: 10.1039/D0TA05500J

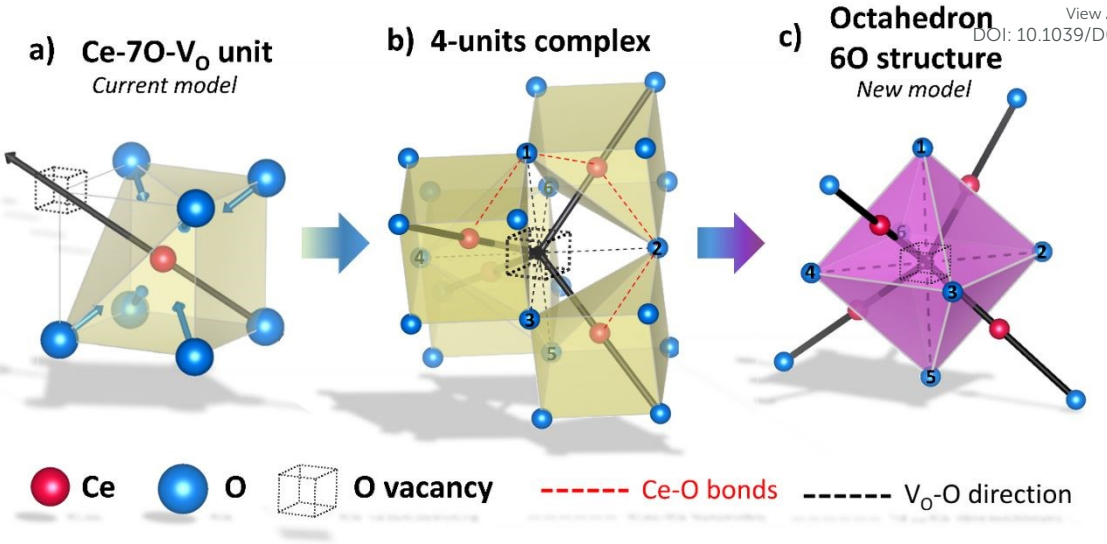

Fig. 1. Vacancy neighbor structure of CeO_2 and related structures. a) Ce_{ce}-7O-$V_{\ddot{O}}$ unit, structure of the current model for electrostriction in CGO. Black vector: $V_{\ddot{O}}$ - Ce_{Ce} - O_O electroactive triplet and distortion direction. Blue vectors: consequent 6O displacement b) 4-units complex composed of four Ce_{ce}-7O-$V_{\ddot{O}}$ distorted units with central vacancy. Near-empty site oxygen atoms, *i.e.* 6O, are numbered. Red lines highlight the bond direction of Ce atoms with oxygen 1 and 2. c) 6O octahedron structure composed of six near-empty site oxygen atoms, base structure for our new model.

Fig. 1a shows the structural model proposed in previous studies to explain the macroscopic distortion of CGO thin films [22]. Using Kröger–Vink notation, we consider a $\boldsymbol{V_{\ddot{O}} - Ce_{Ce}^{\times} - 7O_{\ddot{O}}^{\times}}$ cell, where Ce_{Ce} is the Ce^{4+} cation, $\boldsymbol{V_{\ddot{O}}}$ is a vacancy located in an oxygen site, and $7O_O$ are seven oxygen atoms. when the oxygen vacancy $\boldsymbol{V_{\ddot{O}}}$ is included in a CGO cell (Ce_{ce}-$7O_O$-$\boldsymbol{V_{\ddot{O}}}$), it causes the distortion of the unit, with a consequent rearrangement of the local elastic field and charge distribution. In particular, a distortion takes place by the elongation of the diagonal $\boldsymbol{V_{\ddot{O}}}$ - Ce_{Ce} - O_O triplet (black vector), along the [111] direction. As a counter effect, the other six oxygen atoms, collapse toward the center of the cell (blue vectors). As a consequence, the bonds of $\boldsymbol{V_{\ddot{O}}}$-$Ce_{Ce}$ and Ce_{Ce}-O_O pairs along the diagonal are longer, while the rest Ce_{Ce} - $6O_O$ pairs are shorter. When an electric field is applied, the electroactive $\boldsymbol{V_{\ddot{O}}}$ - Ce_{Ce} - O_O diagonal shrinks, and consequently it "squeezes out" the remaining six oxygen atoms in the perpendicular direction, yielding electrostriction. The model is confirmed by the XAS experiments on thin films [36,37]. Gd doping is needed to introduce a significant concentration of vacancies in the lattice, but it has not an active role on the electrostrictive effect [22,36]. Therefore, Gd was not considered in previous and current models.

According to this interpretation, a field parallel to the [111] direction maximizes the electrostriction effect, as the most efficient way to induce strain of the $\boldsymbol{V_{\ddot{O}}}$-$Ce_{Ce}$-$O_O$ triplets [22,26]. It is worth emphasizing that the model is based on thin films experiments, and it considers only a single cell, neglecting the surrounding structure.

In terms of the crystallographic arrangement, a larger surrounding can be considered in the analysis. Oxygen atoms in CGO lattice have a coordination number of 4, meaning that a single vacancy produces four Ce_{ce}-$7O$-$\boldsymbol{V_{\ddot{O}}}$ units. Fig. 1b shows a schematic illustration of the resulting complex. Under an electric field, all four Ce_{ce}-$7O$-$\boldsymbol{V_{\ddot{O}}}$ units rearrange simultaneously. Particularly, six oxygen atoms (*i.e.* 6O, numbered in Fig. 1b) are bonded to two cations each, as illustrated for atom 1 and 2 (red lines). With an applied field, the 6O are expected to actively contribute to the lattice distortion as they withstand the force of two $\boldsymbol{V_{\ddot{O}}}$ - Ce_{Ce} - O_O triplets at once. Moreover, they are the closest oxygen atoms to the $\boldsymbol{V_{\ddot{O}}}$ site, which is the centre of the local elastic field and charge distortion. The 6O are arranged as an octahedron with the $\boldsymbol{V_{\ddot{O}}}$ site placed in the centre, as illustrated in Fig. 1c.

A similar octahedron structural representation is used to describe the effect of local distortion in piezoelectric ABO_3 perovskites. In such a structure, the oxygen atoms arrange as an octahedron with a centred B-ion that induces stress [45–47]. For piezoelectric perovskites, Li et al. [46,47] also showed a trend of the distortion magnitude as a function of the electric field to the crystalline directions. Such an analysis shows that an electric field parallel to <100> allows oxygen to release the stress imposed by the cation easily along the octahedron axis, favouring atomic distortion. By comparison, the displacement along the <110> directions results in an overall counteracting of the surrounding, leading to a decreased electromechanical response. In the same way, <111> directions show an even weaker distortion effect [46,47]. On the other hand, the trend is the opposite in fluorite structures such as CaF_2 [46].

In this work, we use pulsed laser deposition (PLD) technique to grow (100)-, (110)-, and (111)-oriented CGO grain boundaries free thin films on (100)-oriented $SrTiO_3$ (STO) [2,48], (110) YSZ [48,49] and (100) $NdGaO_3$ (NGO) [48,50,51] respectively. To study the electrostriction effect, we analyze both the longitudinal (M_{11}) and the shear (M_{12}) responses of the films as a function of the crystallographic orientation and the direction of the electric field. Then, we compare the experimental results with the microscopic model based on ABO_3 octahedron applied to CGO. As a result, we are able to provide new

View Article Online
DOI: 10.1039/D0TA05500J

insight into the electrostrictive mechanics in the defective fluorite structure.

Experimental

Film and electrodes deposition

We fabricated $Ce_{0.8}Gd_{0.2}O_{1.9}$ target from powder pressed at 140 MPa and then sintered at 1723 K for 10 h. XRD investigation indicates a pure fluorite phase of the target. One micron thick films of $Ce_{0.8}Gd_{0.2}O_{1.9}$ are grown on $STO_{(100)}$, $NGO_{(100)}$ and $YSZ_{(110)}$ substrates by PLD using a KrF the excimer laser (λ = 248 nm), at 20 Hz repetition rate, 120 mJ energy and fluency of about 1.8 J cm^{-2} (deposition rate was ~0.07 Å/pulse). During the deposition, we fixed the background oxygen pressure at 10^{-3} mbar, with a temperature of 600 °C. Such condition is optimal to grow high-quality fluorite structured CGO with single orientation [2,48]. After deposition, the samples were kept in the chamber with the temperature slowly decreasing (-3°C/min) for reoxidation and release the stress. We sputtered Au top electrodes with a Bal-tec SCD 005 Sputter Coater at room temperature. The substrates' size was 5 x 2.5 mm and 0.1 mm thick.

Samples characterization

We analysed the crystallographic properties of the grown samples using X-ray diffraction with a Rigaku Smartlab diffractometer. We carried out θ-2θ and rocking curve scans, and the crystalline quality of the film was established by evaluating the full-width-half-maximum (FWHM). Grazing incident angle scans with α = 1° were performed on CGO/NGO to exclude the reflection of the substrate, as (100) NGO and (200) CGO reflection overlap at ≈33° and confirm the correct (111) orientation of the film. We analyzed the cross-section of the samples with a Zeiss Gemini-Merlin FE-SEM for microstructure and thickness measurements.

Electrostriction setup

The electromechanical characterization is carried out on a cantilever with planar top electrodes. The samples had one side glued to a base, and the other one free to move. The experiment was performed at room temperature. The method used to calculate the electrostriction coefficient is reported in detail in the Supplementary Information. We performed the measurements with a single-beam laser interferometer SIOS NA analyzer. The experimental setup and instruments are described elsewhere 23. However, we added some new features here described. The interferometer resolution is 5 pm, but the background noise is usually higher, and it is not possible to observe displacements smaller than 3-4 nm. We coupled an Ametek 7230 DSP Lock-in Amplifier to the interferometer. This instrument allows us to extract an oscillating signal from the raw measurement of SIOS NA analyzer. Since lock-in detection spots only periodically signal with a specific set frequency, the measured response is not affected by mechanical drift or external noises. As a consequence, when an oscillating field is applied, the resolution increases to values around 0.1-0.2 nm. These values are used as error bars in our measurements. Supplementary information reports further details of the instrument as well as measurement data as an example (Fig. S2). An AIM-TTI TGP 3100 function generator connected with a Trek 2220 amplifier, are used to apply a sinusoidal electric field to the samples. The voltage amplifier has been added to increase the electric field needed to trigger electrostriction on samples with planar electrodes. The contacts are made with tungsten tips. Oscillation in electrostrictive materials always takes place with double of the frequency of the applied field. For this reason, the source generator and the lock-in amplifier were set at 0.5 Hz and 1 Hz respectively. The displacement measured in this work is always related to the II harmonic contribution to the oscillation amplitude. A schematic of the updated experimental setup is reported in the supplementary information (Fig. S3).

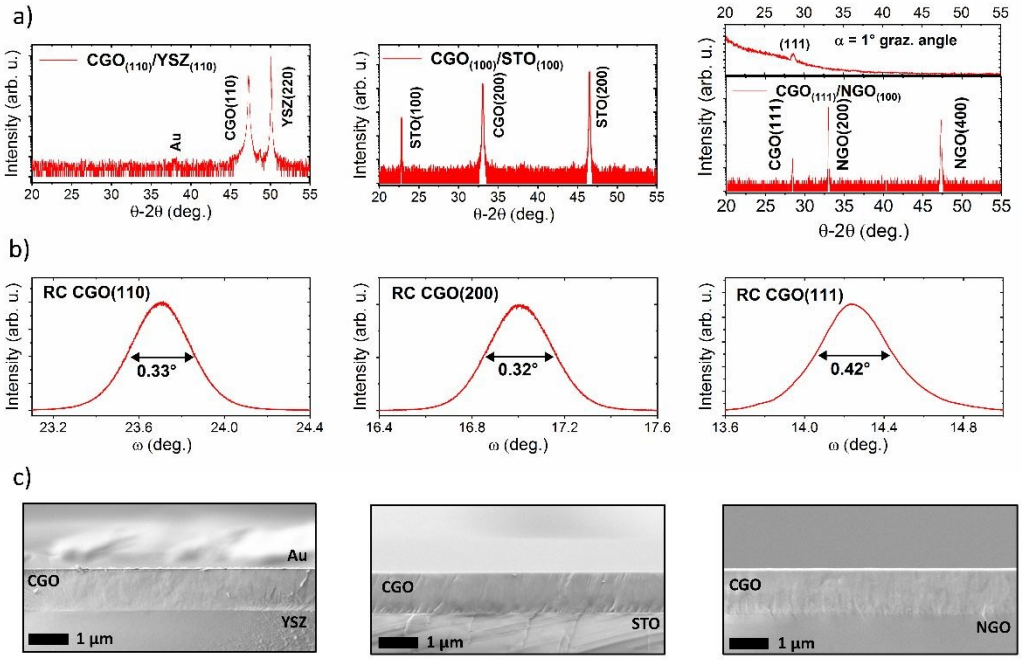

Fig. 2. Structural characterization of $CGO_{(111)}/NGO_{(100)}$, $CGO_{(100)}/STO_{(100)}$ and $CGO_{(110)}/YSZ_{(110)}$ thin films. a) θ-2θ scans of $CGO_{(110)}/YSZ_{(110)}$ at the top, $CGO_{(100)}/STO_{(100)}$ and $CGO_{(111)}/NGO_{(100)}$ at the bottom. *Inset*: θ-2θ scan in grazing angle mode. b) rocking curve at (220) peak of CGO on YSZ, (200) peak of CGO on STO and (111) peak of CGO on NGO. c) cross section images by SEM: from the top $CGO_{(110)}/YSZ_{(110)}$, $CGO_{(100)}/STO_{(100)}$ and $CGO_{(111)}/NGO_{(100)}$.

View Article Online
DOI: 10.1039/D0TA05500J

Results and discussion:

Structural characterization

Fig. 2. Structural characterization of $CGO_{(111)}/NGO_{(100)}$, $CGO_{(100)}/STO_{(100)}$ and $CGO_{(110)}/YSZ_{(110)}$ thin films. a) θ-2θ scans of $CGO_{(110)}/YSZ_{(110)}$ at the top, $CGO_{(100)}/STO_{(100)}$ and $CGO_{(111)}/NGO_{(100)}$ at the bottom. *Inset*: θ-2θ scan in grazing angle mode. b) rocking curve at (220) peak of CGO on YSZ, (200) peak of CGO on STO and (111) peak of CGO on NGO. c) cross-section images by SEM: from the top $CGO_{(110)}/YSZ_{(110)}$, $CGO_{(100)}/STO_{(100)}$ and $CGO_{(111)}/NGO_{(100)}$.

We deposited highly coherent CGO thin films on several single-crystal substrates. Fig. 2 shows the results of both the structural characterization, i.e. XRD pattern in θ-2θ scan mode, rocking curve and the microstructure of the samples thin films by scanning electron microscope (SEM) images. Depending on the orientation of the substrates, the films are grown in a single orientation, i.e. $CGO_{(110)}/YSZ_{(110)}$, $CGO_{(100)}/STO_{(100)}$ and $CGO_{(111)}/NGO_{(100)}$ (Fig. 2a). The inset of $CGO_{(111)}/NGO_{(100)}$ plot shows a grazing angle scan to exclude the presence of CGO (200). For the $CGO_{(200)}/STO_{(100)}$, the cubic cell aligns along the [110] direction of the STO substrate and grows 45° in-plane tilted (Fig. S5) [2], resulting to an epitaxial relationship $<110>_{CGO}//<100>_{STO}$ in both in- and out-of-plane directions.

NGO is a perovskite with an orthorhombic cell. A pseudocubic structure with lattice parameter a ≈ 3.86 Å can be extracted [52]. Considering an NGO substrate with $(200)_{orthorhombic}$ orientation, a good crystallographic match is the (111) face of CGO [50] with in-plane relationship $[001]_{NGO}//[0\text{-}11]_{CGO}$ and $[010]_{NGO}//[\text{-}211]_{CGO}$. Finally, YSZ and CGO have similar cell parameters, CGO grows on (110) YSZ with the in- and out-of-plane relationship $<100>_{CGO}//<100>_{YSZ}$ and $<110>_{CGO}//<110>_{YSZ}$ [48,49]. More details of the film/substrate geometry can be found in the supplementary information. Fig. 2b shows the rocking curve scans of CGO(111)/NGO (100), CGO(100)/STO(100) and CGO(110)/YSZ(110) with FWHM values of 0.42°, 0.32°, and 0.33° respectively. Such low values indicate a high order of crystallinity. The cross-section of films (Fig. 2c) also shows a homogenous and continuous microstructure without the signature of vertical grain boundaries, i.e. columnar grains. The samples are grown with a thickness of t_f = 1µm, ruling out the contribution from substrate-induced strain, which is relieved after a few nanometers [53]. The lattice parameter of the CGO, as determined from the XRD, indicates that the structures are fully relaxed pure fluorite.

Electrostriction effect and discussion

We evaluated the electromechanical performances measuring the longitudinal M_{11} and the transverse M_{12} electrostriction coefficients. We used the cantilever vibration method [23] on samples with in-plane top electrodes (Fig. S1). In $CGO_{(111)}/NGO_{(100)}$, we used two different electrodes configuration, as described in Supplementary Information (Fig. S4). By doing this, we can apply electric field along [-211] and [0-11] directions. In the same way, we apply voltage in $CGO_{(110)}/YSZ_{(110)}$ along [001] and [-223] in-plane directions, as depicted in Fig. S6. Fig. S1b shows a typical map of the 2nd harmonic component of vertical displacement *d* in different positions on the sample. The X-scans and Y-scans indicate a distortion both parallel and perpendicular to the electric field, respectively.

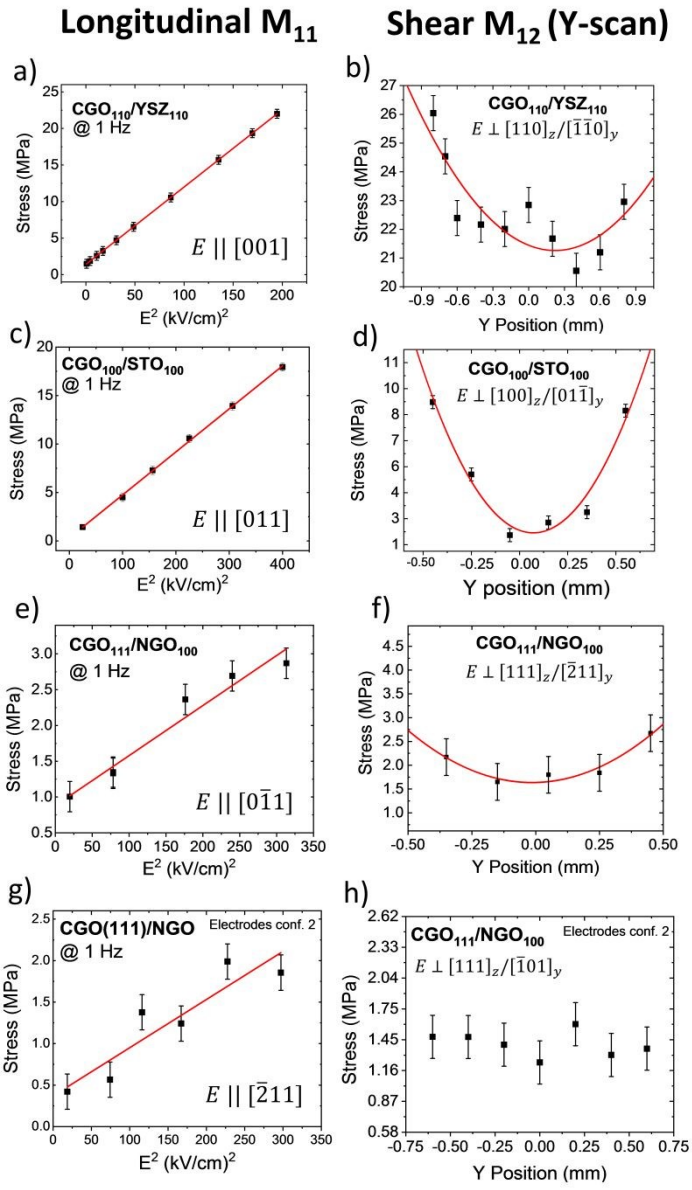

Fig. 3. Electromechanical response of CGO thin films for different orientations and electric field direction, II harmonic of oscillation @ 1 Hz. First row: CGO (110) oriented on YSZ with electric field along [001] axis. *b)* Longitudinal stress vs electric field, M_{11}, *c)* Y-scan of displacement. *d)* Octahedron model geometry with directions of the electric field (red arrow) and crystal orientation (black arrow) displayed. Second row: CGO (100) on STO with $\vec{E}$ ∥ [011]. *e)* Longitudinal stress, *f)* shear displacement and *g)* octahedron model. Third row: CGO (111) on NGO with $\vec{E}$ ∥ [0-11]. *h)* Longitudinal stress, *i)* shear displacement and *l)* octahedron model. Fourth row: CGO (111) on NGO with $\vec{E}$ ∥ [-211]. *m)* Longitudinal stress, *n)* shear displacement and *o)* octahedron model.

View Article Online
DOI: 10.1039/D0TA05500J

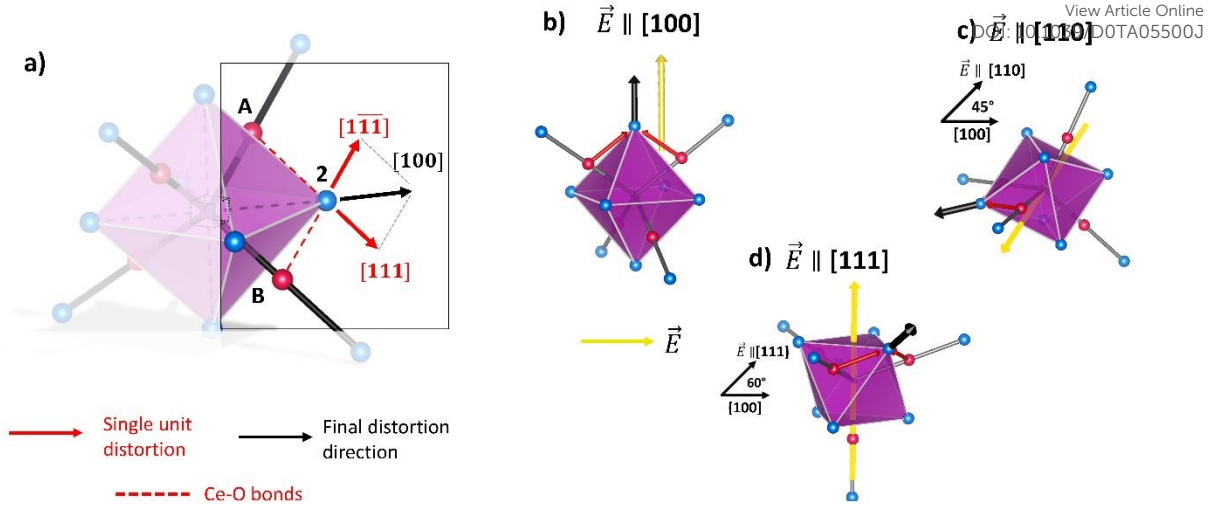

Fig. 4. Microscopic interpretation of CGO electrostriction in $V_O^{\bullet\bullet}$ neighborhood lattice. *a)* 4-units complex with $V_O^{\bullet\bullet}$- Ce_{Ce} - O_O triplets imposed stress. *b)* Preferred direction in octahedron structure parallel with electric field along [100] direction. *c)* Preferred direction (black line) compared to induced stress with an electric field (yellow line) along [110] with an angle of 45° *d)* Preferred direction with electric field parallel to [111] with a 60° angle.

To measure the longitudinal electrostriction coefficient M_{11}, we measure the displacement *d* in a fixed position for different electric fields. The scans along the width of the sample (Y-scans) allow evaluating the shear component M_{12} (see the experimental section for details).

Fig. 3 shows the electromechanical response of CGO thin films for both longitudinal and shear directions. Indications of the electric field direction are also reported. Fig. 3a shows the performances of $CGO_{(110)}/YSZ_{(110)}$ in response to the electric field along [001] direction. The longitudinal electrostriction coefficient is found to be M_{11} = $4.93{\cdot}10^{-17}$ m^2V^{-2}. Fig. 3c,e show the response of $CGO_{(100)}/STO_{(100)}$ and $CGO_{(111)}/NGO_{(100)}$ to the electric field along [110] direction with a longitudinal electrostriction coefficient of $2.22{\cdot}10^{-17}$ m^2V^{-2} and $3.50{\cdot}10^{-18}$ m^2V^{-2}, respectively. Fig. 3g shows the electric field in $CGO_{(111)}/NGO_{(100)}$ sample with in-plane electrodes is along [-211] direction with an M_{11} = $2.03{\cdot}10^{-18}$ m^2V^{-2}. In $CGO_{(110)}/YSZ_{(110)}$ with electrodes along the [-223] direction, the electrostriction is annihilated, and the oscillations are so weak to be comparable with the background noise. Therefore, we cannot calculate the electrostriction coefficient, and we report it as minimal noise value M_{11} = $<6.72{\cdot}10^{-19}$ m^2V^{-2}. Each measurement lasted between 5 and 10 minutes. We did not find evidence of degeneration of performances with time, evidencing sound mechanical integrity of the device [23].

According to equation S4, the electrostriction coefficient is dependent on CGO Young´s modulus (Y), which we assumed 200 GPa [22,23,53–55]. Y values can change depending on the *hkl* texture, but such measurements are still not available in the literature. However, Goldsby et al. reported the elastic compliances of CeO_2 by the first-principle simulation for different *hkl* [56], showing a maximum difference of 30% from the average value. Moreover, Young´s modulus was obtained in fluorite structure YSZ [57,58], showing similar values along with all the crystal directions. Kurpaska et al. in particular, reported Y ranging from 235 GPa along <110> to 216 GPa along with <111>[58]. Fujikane et al., on the other hand, showed variable Y depending on the experimental technique. They considered the nanoindentation method as the most trustable as they obtained Y with a maximum difference of 21% or 9% for elastic and elastoplastic deformation, respectively. Taking into account these results, we decided to use the approximated Y presented in the literature for thin-film configuration.

Fig. 3b, d, f, h show the full Y-scans for M_{12} analysis as a result of laser profilometry measurements. We applied 13 kV/cm at 1 Hz of frequency. The transverse electrostriction coefficient represents the component of stress that is perpendicular to the electric field. As the electrostriction effect takes place at both in- and out- of plane directions, we describe the crystal distortion in terms of vertical and lateral directions. Fig. 3b shows the transverse electrostrictive response of $CGO_{(110)}/YSZ_{(110)}$ with a measured value of M_{12} = $0.26{\cdot}10^{-17}$ m^2V^{-2} considering the vertical (*z*) and in-plane (*y*) directions $[110]_z$ / $[\text{-}1\text{-}10]_y$. On other hand, for the $CGO_{(100)}/STO_{(100)}$ sample, the electrostriction coefficient is $M_{12} = 0.79{\cdot}10^{-17}$ m^2V^{-2} along $[100]_z$ / $[0\text{-}11]_y$ as depicted in Fig. 3d. $CGO_{(111)}/NGO_{(100)}$ shows an electrostriction coefficient of M_{12} = $1.9{\cdot}10^{-18}$ for $[111]_z$ / $[\text{-}211]_y$ directions. Finally, $CGO_{(111)}/NGO_{(100)}$ with $[111]_z$ / $[\text{-}101]_y$ perpendicular directions does not show a clear parabolic profile along the width.

Our measurements deviate from the prediction of the single-cell model described by Yavo *et al.* [22,36,37], which suggests that the distortion is favoured if the electric field is along the [111] direction (see Fig. 1a). We propose here an alternative view of the effect, based on the previous one, but extended to the octahedron structure and supported by our experimental results. It is worth noticing that our interpretation is not necessarily in contrast with the model previously reported, as the primary effect is the same. We consider the broad environment of the oxygen vacancy and the anisotropic behaviour of electrostriction expands beyond the single-cell.

Fig. 4a shows the octahedron structure. Each of the oxygen atoms depicted withstands distortions from two $V_O^{\bullet\bullet}$ - Ce_{Ce} - O_O triplets. As an example, the oxygen atom labelled as 2 (highlighted in the figure) is strained by the triplets labelled as A and B. Both displacements take place along diagonal directions, as depicted by the reds arrows. Consequently, the resulting distortion is parallel to [100] direction

View Article Online
DOI: 10.1039/D0TA05500J

	ORIENTATION ∥ $\vec{E}$	LONGITUDINAL M_{11} (m^2/V^2)	ORIENTATION ⊥ $\vec{E}$	SHEAR M_{12} (m^2/V^2)
CGO_{110}/YSZ_{110}	[001]	4.93 (9.11) ·10^{-17}	[a)][110]$_z$ / [-1-10]$_y$	0.26·10^{-17}
CGO_{100}/STO_{100}	[011]	2.22 (2.45) ·10^{-17}	[100]$_z$ /[01-1]$_y$	0.79·10^{-17}
CGO_{111}/NGO_{100}	[0-11]	3.50·10^{-18}	[111]$_z$ / [-211]$_y$	1.9·10^{-18}
CGO_{111}/NGO_{100}*	[-211]	2.03·10^{-18}	[111]$_z$ / [-101]$_y$	//
CGO_{110}/YSZ_{110}**	[-223]	<6.72·10^{-19}	[110]$_z$ / [-33-4]$_y$	//

Tab. 1. Longitudinal (M11) and shear (M12) electrostriction coefficient of CGO thin films depending on electric field direction and perpendicular orientation. a) (z and y denote the vertical and lateral orientation of the films, respectively). The values in the brackets are values calculated without subtracting the contribution of substrates (Fig. S7-8-9). *, **: el. conf. 2 (suppl. info).

(black lines), corresponding with the octahedron axis. We approximate the stress to have the same intensity for all triplets. As a result, when an electric field is aligned with the <100> directions, the atomic displacement is maximized because it is parallel to the favoured distortion directions (Fig. 4b). When the field is applied along a non-preferential direction, the distortion decreases as the angle respect to the preferred direction increases. In particular, <110> and <111> directions have an angle 45° and 60° respectively (Fig. 4c, d). Again, the same relation between distortion magnitude and crystal direction is found in the microscopic model for ABO_3 perovskites [45–47]. In summary, CGO electrostriction can be described by an *"octahedron model", i.e.* distortion of 6O atoms octahedron with central $\mathbf{V_O^{\bullet\bullet}}$, in which the electroactive forces are mediated by the $\mathbf{V_O^{\bullet\bullet}}$ - Ce_{Ce} - O_O triplets. The preferential directions of atomic distortion are along <100>, followed by <110> and then <111>, with the electromechanical performances following this trend. Interestingly, these results suggest that the geometric properties of CGO electrostriction are similar to perovskite structures rather than regular fluorites such as CaF_2, which preferred distortion is along <111> [46]. As the force applied from each triplet to one oxygen can be different, an asymmetric contribution to the overall distortion could take place. Moreover, a contribution from the oxygen atoms outside the octahedron can play a role.

The M_{11} values follow the trend expected from the octahedron model. The highest electromechanical performances are found in $CGO_{(110)}/YSZ_{(110)}$ sample for fields applied along <100>, intermediate performances for <110> directions in $CGO_{(100)}/STO_{(100)}$ and lower performances for diagonal direction [-211] in $CGO_{(111)}/NGO_{(100)}$. The M_{12} values are considerably lower than longitudinal coefficients but, considering both in-plane (*y*) and vertical (*z*) directions, the performances of the samples consistently follow the trend expected from the model. Tab. 1 summarizes the results for the longitudinal and the transverse electrostriction coefficients at different crystal directions. Despite having lower M_{11} compared to $CGO_{(110)}/YSZ_{(110)}$, the $CGO_{(100)}/STO_{(100)}$ sample shows an M_{12} value of about three times higher. In CGO_{100}/STO_{100} the out-of-plane distortion takes place along $[100]_z$, which allows an easy releasing of the stress compared to $[110]_z$ direction in CGO_{110}/YSZ_{110}, resulting thus in a more significant electrostriction coefficient. Remarkably, the M_{11} of the $CGO_{(100)}/STO_{(100)}$ and $CGO_{(111)}/NGO_{(100)}$ samples show a difference despite having the field applied along with directions of the same family: [011] and [0-11] respectively (Fig. 3f,h). We explained this effect by assuming that the weaker transverse effect of $CGO_{(111)}/NGO_{(100)}$ influences the longitudinal performances.

Conclusions

In this work, we fabricate highly coherent CGO thin films with (100), (110) and (111) orientation. These films are electromechanical tested using a planar electrodes geometry at different electric field directions for both longitudinal (M_{11}) and transverse (M_{12}) directions. The electrostrictive performances depend on the crystalline direction of the film, showing a maximum value of $M_{11} = 4.93 \cdot 10^{-17}$ m^2V^{-2} along <100> direction, followed by <110> and then <111>. To support the experimental results, we propose an extension of the current model, based on the octahedron structure of oxygen atoms neighbour of a $\mathbf{V_O^{\bullet\bullet}}$ site. By such an interpretation, we explain the reason for the performance trend concerning crystal direction, giving new insight into the microscopic mechanism behind electrostriction in CGO.

Conflicts of interest

There are no conflicts to declare.

Acknowledgements

This research was supported by the Danish Council for Independent Research Technology and Production Sciences for the DFF- Research Project 2 (Grant No. 48293) and the BioWings project funded by the European Union's Horizon 2020, Future and Emerging Technologies (FET) programme (Grant No. 801267).

References:

1 V. Esposito and E. Traversa, *J. Am. Ceram. Soc.*, 2008, **91**, 1037–1051.

2 S. Sanna, V. Esposito, D. Pergolesi, A. Orsini, A. Tebano, S. Licoccia, G. Balestrino and E. Traversa, *Adv. Funct. Mater.*, 2009, **19**, 1713–1719.

3 C. Sun, H. Li and L. Chen, *Energy Environ. Sci.*, 2012, **5**, 8475–8505.

4 P. Jasinski, T. Suzuki and H. U. Anderson, *Sensors Actuators, B Chem.*, 2003, **95**, 73–77.

5 M. Kuhn, S. R. Bishop, J. L. M. Rupp and H. L. Tuller, *Acta Mater.*, 2013, **61**, 4277–4288.

6 J. Kas, P. Fornasiero and M. Graziani, *Catal. Today*, 1999, **50**, 285–298.

7 N. Yang, Y. Shi, S. Schweiger, E. Strelcov, A. Belianinov, V. Foglietti, P. Orgiani, G. Balestrino, S. V. Kalinin, J. L. M. Rupp and C. Aruta, *ACS Appl. Mater. Interfaces*, 2016, **8**, 14613–14621.

8 A. Younis, D. Chu, X. Lin, J. Yi, F. Dang and S. Li, *ACS Appl. Mater. Interfaces*, 2013, **5**, 2249–2254.

9 S. Schweiger, M. Kubicek, F. Messerschmitt, C. Murer and J. L. M. Rupp, *ACS Nano*, 2014, **8**, 5032–5048.

10 R. Schmitt, J. Spring, R. Korobko and J. L. M. Rupp, *ACS Nano*, 2017, **11**, 8881–8891.

11 N. Pryds and V. Esposito, *J. Electroceramics*, 2017, **38**, 1–23.

12 K. Rodrigo, S. Heiroth, M. Lundberg, N. Bonanos, K. Mohan Kant, N. Pryds, L. Theil Kuhn, V. Esposito, S. Linderoth, J. Schou and T. Lippert, *Appl. Phys. A Mater. Sci. Process.*, 2010, **101**, 601–607.

13 K. M. Kant, V. Esposito and N. Pryds, *Appl. Phys. Lett.*, 2010, **97**, 5–8.

14 M. Melchionna and P. Fornasiero, *Mater. Today*, 2014, **17**, 349–357.

15 S. Ackermann and A. Steinfeld, *J. Phys. Chem*, 2014, 5216−5225.

16 I. Kosacki, T. Suzuki, V. Petrovsky and H. U. Anderson, *Solid State Ionics*, 2000, **136–137**, 1225–1233.

17 K. Mohan Kant, V. Esposito and N. Pryds, *Appl. Phys. Lett.*, , DOI:10.1063/1.3676659.

18 S. Wang, T. Kobayashi, M. Dokiya and T. Hashimoto, *J. Electrochem. Soc.*, 2000, **147**, 3606.

19 G. Baure, R. M. Kasse, N. G. Rudawski and J. C. Nino, *Phys. Chem. Chem. Phys.*, 2015, **17**, 12259–12264.

20 T. S. Stefanik and H. L. Tuller, *J. Electroceramics*, 2004, **13**, 799–803.

21 S. R. Bishop, T. S. Stefanik and H. L. Tuller, *Phys. Chem. Chem. Phys.*, 2011, **13**, 10165–10173.

22 R. Korobko, A. Patlolla, A. Kossoy, E. Wachtel, H. L. Tuller, A. I. Frenkel and I. Lubomirsky, *Adv. Mater.*, 2012, **24**, 5857–5861.

23 S. Santucci, H. Zhang, S. Sanna, N. Pryds and V. Esposito, *APL Mater.*, 2019, **7**, 071104.

24 R. Korobko, E. Wachtel and I. Lubomirsky, *Sensors Actuators, A Phys.*, 2013, **201**, 73–78.

25 A. D. Ushakov, N. Yavo, E. Mishuk, I. Lubomirsky, V. Y. Shur and A. L. Kholkin, *KnE Mater. Sci.*, 2016, **1**, 177.

26 M. Hadad, H. Ashraf, G. Mohanty, C. Sandu and P. Muralt, *Acta Mater.*, 2016, **118**, 1–7.

27 A. Kabir, S. Santucci, N. Van Nong, M. Varenik, I. Lubomirsky, R. Nigon, P. Muralt and V. Esposito, *Acta Mater.*, 2019, **174**, 53–60.

28 N. Yavo, O. Yeheskel, E. Wachtel, D. Ehre, A. I. Frenkel and I. Lubomirsky, *Acta Mater.*, 2018, **144**, 411–418.

29 E. Mishuk, E. Makagon, E. Wachtel, S. R. Cohen, R. Popovitz-Biro and I. Lubomirsky, *Sensors Actuators, A Phys.*, 2017, **264**, 333–340.

30 A. D. Ushakov, E. Mishuk, E. Makagon, D. O. Alikin, A. A. Esin, I. S. Baturin, A. Tselev, V. Y. Shur, I. Lubomirsky and A. L. Kholkin, *Appl. Phys. Lett.*, 2017, **110**, 142902.

31 E. Mishuk, A. D. Ushakov, S. R. Cohen, V. Y. Shur, A. L. Kholkin and I. Lubomirsky, *Solid State Ionics*, 2018, **327**, 47–51.

32 R. E. N. V. Sundar, J.-F. Li, D. Viehland, *Mater. Res. Bull.*, 1996, **31**, 555–563.

33 R. E. Newnham, V. Sundar, R. Yimnirun, J. Su and Q. M. Zhang, *J. Phys. Chem. B*, 1997, **101**, 10141–10150.

34 N. Yavo, A. D. Smith, O. Yeheskel, S. Cohen, R. Korobko, E. Wachtel, P. R. Slater and I. Lubomirsky, *Adv. Funct. Mater.*, 2016, **26**, 1138–1142.

35 S. Kim and J. Maier, *J. Electrochem. Soc.*, 2002, **149**, J73.

36 R. Korobko, A. Lerner, Y. Li, E. Wachtel, A. I. Frenkel and I. Lubomirsky, *Appl. Phys. Lett.*, 2015, **106**, 042904.

37 Y. Li, O. Kraynis, J. Kas, T. C. Weng, D. Sokaras, R. Zacharowicz, I. Lubomirsky and A. I. Frenkel, *AIP Adv.*, , DOI:10.1063/1.4952645.

38 L. Sun, D. Marrocchelli and B. Yildiz, *Nat. Commun.*, 2015, **6**, 1–10.

39 Y. Lei, Y. Ito, N. D. Browning and T. J. Mazanec, *J. Am. Ceram. Soc.*, 2002, **85**, 2359–2363.

40 S. Kim, P. Jain, H. J. Avila-Paredes, A. Thron, K. Van Benthem and S. Sen, *J. Mater. Chem.*, 2010, **20**, 3855–3858.

41 Y. L. Kuo, C. Lee, Y. S. Chen and H. Liang, *Solid State Ionics*, 2009, **180**, 1421–1428.

42 H. J. Avila-Paredes, K. Choi, C. T. Chen and S. Kim, *J. Mater. Chem.*, 2009, **19**, 4837–4842.

43 A. Infortuna, A. S. Harvey and L. J. Gauckler, *Adv. Funct. Mater.*, 2008, **18**, 127–135.

44 A. Kossoy, Q. Wang, R. Korobko, V. Grover, Y. Feldman, E. Wachtel, A. K. Tyagi, A. I. Frenkel and I. Lubomirsky, *Phys. Rev. B*, 2013, **87**, 054101.

45 K. Uchino, S. Nomura, L. E. Cross, R. E. Newnham and S. J. Jang, *J. Mater. Sci.*, 1981, **16**, 569–578.

46 F. Li, L. Jin, Z. Xu and S. Zhang, *Appl. Phys. Rev.*, , DOI:10.1063/1.4861260.

47 F. Li, L. Jin, Z. Xu, D. Wang and S. Zhang, *Appl. Phys. Lett.*, , DOI:10.1063/1.4802792.

48 S. Sanna, V. Esposito, A. Tebano, S. Licoccia, E. Traversa and G. Balestrino, *Small*, 2010, **6**, 1863–1867.

49 R. Sinclair, S. C. Lee, Y. Shi and W. C. Chueh, *Ultramicroscopy*, 2017, **175**, 25–35.

50 L. Chen, C. L. Chen, D. X. Huang, Y. Lin, X. Chen and A. J. Jacobson, *Solid State Ionics*, 2004, **175**, 103–106.

51 N. Yang, P. Orgiani, E. Di Bartolomeo, V. Foglietti, P. Torelli,

View Article Online
DOI: 10.1039/D0TA05500J

A. V. Ievlev, G. Rossi, S. Licoccia, G. Balestrino, S. V. Kalinin and C. Aruta, *J. Phys. Chem. C*, 2017, **121**, 8841–8849.

52 M. Mathews, E. P. Houwman, H. Boschker, G. Rijnders and D. H. A. Blank, *J. Appl. Phys.*, 2010, **107**, 013904 1–5.

53 Y. Shi, S. C. Lee, M. Monti, C. Wang, Z. A. Feng, W. D. Nix, M. F. Toney, R. Sinclair and W. C. Chueh, *ACS Nano*, 2016, **10**, 9938–9947.

54 A. Selçuk and A. Atkinson, *J. Eur. Ceram. Soc.*, 1996, **17**, 1523–1532.

55 R. Korobko, C. T. Chen, S. Kim, S. R. Cohen, E. Wachtel, N. Yavo and I. Lubomirsky, *Scr. Mater.*, 2012, **66**, 155–158.

56 J. C. Goldsby, *J. Ceram.*, 2012, **2013**, 1–4.

57 M. Fujikane, D. Setoyama, S. Nagao, R. Nowak and S. Yamanaka, *J. Alloys Compd.*, 2007, **431**, 250–255.

58 L. Kurpaska, M. Frelek-Kozak, K. Nowakowska-Langier, M. Lesniak, J. Jasinski and J. Jagielski, *Nucl. Instruments Methods Phys. Res. Sect. B Beam Interact. with Mater. Atoms*, 2017, **409**, 81–85

DOI: 10.1039/D0TA05500J

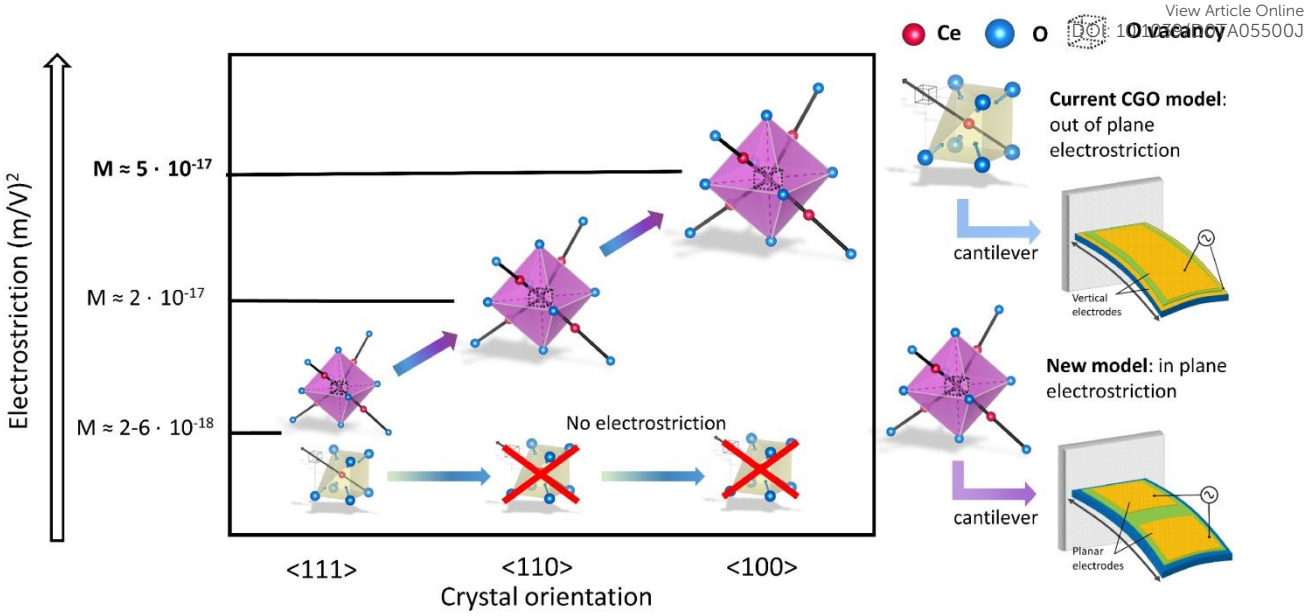

Gd-doped ceria electrostriction enhanced: The electrostriction effect in Gd-doped ceria is commonly thought to be maximum along <111> crystallographic directions as a result of a microscopic model. Based on experimental results on thin films with controlled in and out of plane orientation, this study uncovers new anisotropic properties of the effect, which is enhanced along with the <100> crystallographic directions by roughly one order of magnitude. Thus, we propose a new extended microscopical model to explain such new findings.